Article

Journal of Vibration and Control
2016, Vol. 22(6) 1633–1644

DOI: 10.1177/1077546314543911
jvc.sagepub.com

Airfoil control surface discontinuous nonlinearity experimental assessment and numerical model validation

Rui MG Vasconcellos[1], Abdessattar Abdelkefi[2], Muhammad R Hajj[2], Daniel P Almeida[3] and Flávio D Marques[3]

Abstract

A variety of dynamic behaviors that may be encountered in aeroelastic systems with discontinuous nonlinearities has motivated investigations that may support future applications in flight controls design, flutter prediction, instability characterization and energy harvesting. In this paper, the case of an airfoil with control surface freeplay is assessed experimentally and modeled numerically using an alternative continuous approximation for the discontinuous nonlinearity based on hyperbolic tangent function representation. The unsteady aerodynamic loads are computed using the modified unsteady Theodorsen approximation for arbitrary motions. The validity of the proposed freeplay representation is performed through comparison with experimental data. Adjustments to the pitching restoring moments have been carried out to account for a smooth polynomial concentrated nonlinearity. Data analysis is performed to characterize and investigate the experimental signals. Sub-critical bifurcation behavior is observed from both experimental data and the numerical model prediction. The results confirm the validity of hyperbolic tangent function combinations for freeplay nonlinearity representation for the experimental setup conditions.

Keywords

Experimental aeroelasticity, freeplay, nonlinear dynamics, time series analysis, bifurcation

1. Introduction

Nonlinear aeroelastic responses may result in undesirable instabilities such as flutter, limit cycle oscillations (LCOs), and bifurcations leading to nonperiodic or chaotic motions. Aeroelastic nonlinearities can manifest either from unsteady aerodynamics or structural sources. Notoriously, structural nonlinearities occur due to many factors such as large structural deflections, material behavior, partial loss of structural integrity (aging or incidents), and gaps or imperfections in links or joints. Moreover, a certain amount of freeplay associated with moving control surface hinges or external store links is inevitable.

Lee and Tron (1989) have shown that freeplay nonlinearities can lead to chaotic motions, confirmed by Vasconcellos et al. (2012). Another relevant modeling of freeplay nonlinearity effects on the control surface of a typical aeroelastic section has been presented by Conner et al. (1996) and Trickey et al. (2002). Li et al. (2010) have also studied control surface freeplay with the influence of adding a cubic nonlinearity in the typical section pitch stiffness, which leads to LCO at speeds higher than the flutter speed.

Virgin et al. (1999), Conner et al. (1996), and Trickey et al. (2002) have associated freeplay non-linear effects with transitions from damped, to periodic LCOs, to quasi-periodic aeroelastic responses, and then to chaotic motions in experimental tests. Those experimental results have become a relevant source of information

[1]São Paulo State University - UNESP, São João da Boa Vista, SP, Brazil
[2]Department of Engineering Science and Mechanics, Virginia Polytechnic Institute and State University, Blacksburg, VA, USA
[3]Engineering School of São Carlos, University of São Paulo, São Carlos, SP, Brazil

Received: 15 October 2013; accepted: 3 May 2014

Corresponding author:
Flávio D Marques, Engineering School of São Carlos, University of São Paulo, Av. Trabalhador Sancarlense, 400, 13566-590, São Carlos, SP, Brazil.
Email: fmarques@sc.usp.br

related to nonlinear aspects of aeroelastic systems with freeplay. In most of the cases, transitions have been observed at speeds lower than that of linear flutter speed. Using a discontinuous function to represent the freeplay nonlinearity and following the Henon's method (Henon, 1982), Conner et al. (1996) have identified the transitional points using a typical section mathematical model. The Henon's method has been conceived to search points in Poincaré mappings and it is usually known as the technique of inverse interpolation. Nonetheless, it can be applied to achieve time-integration of equations of motion of dynamical systems with any form of discrete nonlinearity. However, to perform a complete analysis, this method requires multiple time-integrations at small time steps, thereby increasing computation effort. Alternative techniques to overcome this drawback have also been developed (Jones et al., 2007; Roberts et al., 2002). Although these approaches can generate better results, in comparison with traditional ones, these methods are still time intensive.

Recently, Vasconcellos et al. (2012) have compared numerical simulations of a typical section where freeplay modeling assumptions are considered in the control surface hinge. Conventional time-integration has been used and the freeplay effect has been represented in terms of discontinuous function, polynomial forms, and with a combination of hyperbolic tangent function. Simulations, in this case, have been performed taking into account the experimental results from Conner et al. (1996). The results from Vasconcellos et al. (2012) have shown that the hyperbolic tangent function combination approach for modeling discontinuous nonlinearities is appropriate for detecting different nonlinear behaviors, including the experimentally observed LCO, chaos and transitions. Moreover, such freeplay representation has also reduced the required computational time, thereby accelerating the aeroelastic simulations.

The aim of this paper is to present an investigation on the validity of hyperbolic tangent representation of control surface freeplay nonlinearity with new experimental data at different conditions of those already checked in previous works (Vasconcellos et al., 2012). Wind tunnel experimental tests have been performed to allow data comparable to a typical section model. During experimental procedure other sources of nonlinearities, particularly in pitching, have also been observed and characterized to improve the numerical model prediction. Damping effects are also included in terms of damping factors estimation from dynamic measurements. The numerical aeroelastic model has been assessed with linear aerodynamics based on Theodorsen formulation, and freeplay represented by hyperbolic tangent function combination. Time-integration of the aeroelastic equations of motion has been preformed with traditional Runge–Kutta method. Results have confirmed the efficiency of the alternative freeplay representation.

2. Experimental setup

The aeroelastic tests have been carried out using an open-circuit blower wind tunnel with $0.5\,\text{m} \times 0.5\,\text{m}$ output cross-section and capable of maximum air velocity of approximately 17.0 m/s (cf. Figure 1(a)). The experimental apparatus has been conceived to reproduce the typical airfoil section aeroelastic behavior in incompressible flow.

The airfoil has been built of a foam–aluminum–fiberglass wing (span of 0.6 m) that is mounted vertically at the $\frac{1}{4}$ chord from leading edge by using an aluminum shaft. The shaft is connected at its top and bottom, through bearings to a support where both pitching and plunging mechanisms are attached. The plunge suspension is a bi-cantilever beam made of two steel leaf-springs. The torsional pitch stiffness comprises a steel leaf-spring inserted tightly into a slot in

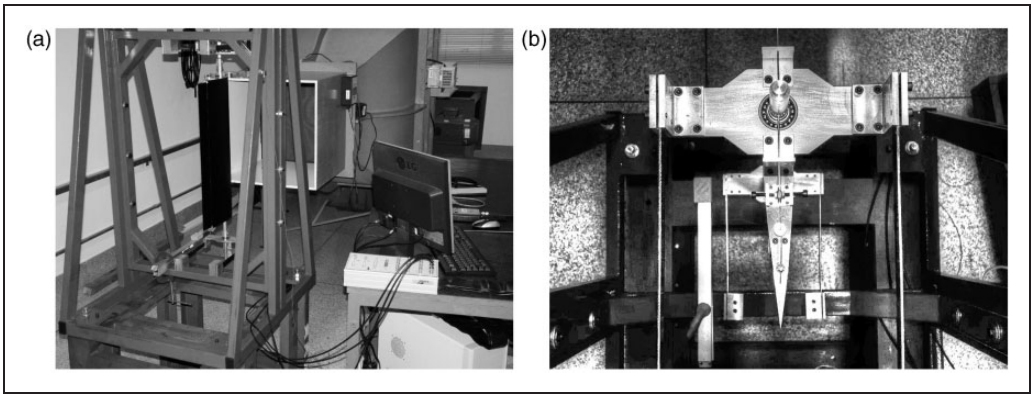

Figure 1. Experimental set-up and details of the airfoil suspension: (a) wind tunnel set-up; (b) plunge suspension details (top view).

the main shaft. The free end of the leaf-spring is placed into a support. The distance between the shaft and support and the thickness of the leaf-springs can also be changed to vary the stiffness. The airfoil center of gravity can be adjusted chordwise with the addition of balance weights. A control surface is attached to the main wing by two low-friction micro-bearings. The control surface stiffness depends on a spring wire inserted in the shaft. The free tip of spring wire is placed in such a way that a gap exists, thereby allowing freeplay at a certain range.

The parameters used for experimental procedure have been tuned to meet the wind tunnel, sensors, and acquisition system limitations. The aeroelastic system parameters are presented in Table 1 (these are related to the aeroelastic model described in Section 3), while photos of the experimental setup with details are presented in Figures 1 and 2. Experimental data have been acquired with angular encoders for pitching and control surface motions. The plunge motion has been acquired with a linear encoder. Data acquisition has been processed using DSpace® DS1104 and Matlab/Simulink®.

3. Nonlinear aeroelastic model

The aeroelastic system is modeled considering the typical section with a trailing edge control surface as illustrated in Figure 3, where b is the semi-chord, a is the elastic axis position in semi-chords with respect to the mid-chord, c is the distance from mid-chord of the control surface hinge in semi-chords, α is the pitch angle, β is the angle of the control surface, w is the plunge displacement and U is the free-stream velocity, k_α, k_β and k_w are used to represent, respectively, the pitch, control surface and bending stiffness.

Table 1. Typical aeroelastic section experimental parameters (description in Section 3).

b	0.125 m
a	–0.5
c	0.5
ρ	1.0844 kg/m^3
m_W	1.51 kg
m_T	3.67 kg
ω_h	30.72 rad/s
ω_α	17.16 rad/s
ω_β	62.58 rad/s
x_α	0.66
x_β	0.0028
r_α^2	0.533
r_β^2	0.0055
μ	28.18

Aeroelastic equations of motion can be derived using the traditional methods (Fung, 1993) and added nonlinear representation to structural stiffness, which leads to

$$\begin{bmatrix} m_W b^2 r_\alpha^2 & m_W b^2 r_\beta^2 + m_W b^2 x_\beta (c-a) & m_W b x_\alpha \\ m_W b^2 r_\beta^2 + m_W b^2 x_\beta (c-a) & m_W b^2 r_\beta^2 & m_W b x_\beta \\ m_W b x_\alpha & m_W b x_\beta & m_T \end{bmatrix} \times \begin{Bmatrix} \ddot{\alpha} \\ \ddot{\beta} \\ \ddot{w} \end{Bmatrix} + \begin{bmatrix} d_{\alpha\alpha} & d_{\alpha\beta} & d_{\alpha w} \\ d_{\beta\alpha} & d_{\beta\beta} & d_{\beta w} \\ d_{w\alpha} & d_{w\beta} & d_{ww} \end{bmatrix} \begin{Bmatrix} \dot{\alpha} \\ \dot{\beta} \\ \dot{w} \end{Bmatrix} + \begin{bmatrix} m_W b^2 r_\alpha^2 \omega_\alpha^2 F(\alpha) & 0 & 0 \\ 0 & m_W b^2 r_\beta^2 \omega_\beta^2 F(\beta) & 0 \\ 0 & 0 & m_W \omega_w^2 F(w) \end{bmatrix} \begin{Bmatrix} \alpha \\ \beta \\ w \end{Bmatrix} = \begin{Bmatrix} M_\alpha(t) \\ M_\beta(t) \\ -L(t) \end{Bmatrix}, \tag{1}$$

where m_W and m_T are the wing mass and total mass (wing plus elastic suspension moving masses), r_α and r_β are the radii of gyration, respectively, in pitching and for the control surface, x_α is the distance between the elastic axis and the center of gravity, x_β is the distance of the control surface hinge to the control surface center of gravity, d_{ij} are damping coefficients with respect to each airfoil motion and their influences (Rayleigh approach), ω_α, ω_β, and ω_w are used to represent, respectively, the pitch, control surface, and bending decoupled natural frequencies, $F(\alpha)$, $F(\beta)$, and $F(w)$ are functions to represent nonlinear structural stiffness, $M_\alpha(t)$, $M_\beta(t)$, and $L(t)$ are unsteady pitching moment, control surface hinge moment, and lift force, respectively.

Aerodynamic loading can be computed using the Theodorsen (1935) approach, where the unsteady aerodynamic forces and moments are calculated using the linearized potential flow, thin airfoil theory and written respectively as

$$L(t) = L^{(nc)} + L^{(c)}, \tag{2}$$

$$M_\alpha(t) = M_\alpha^{(nc)} + M_\alpha^{(c)}, \tag{3}$$

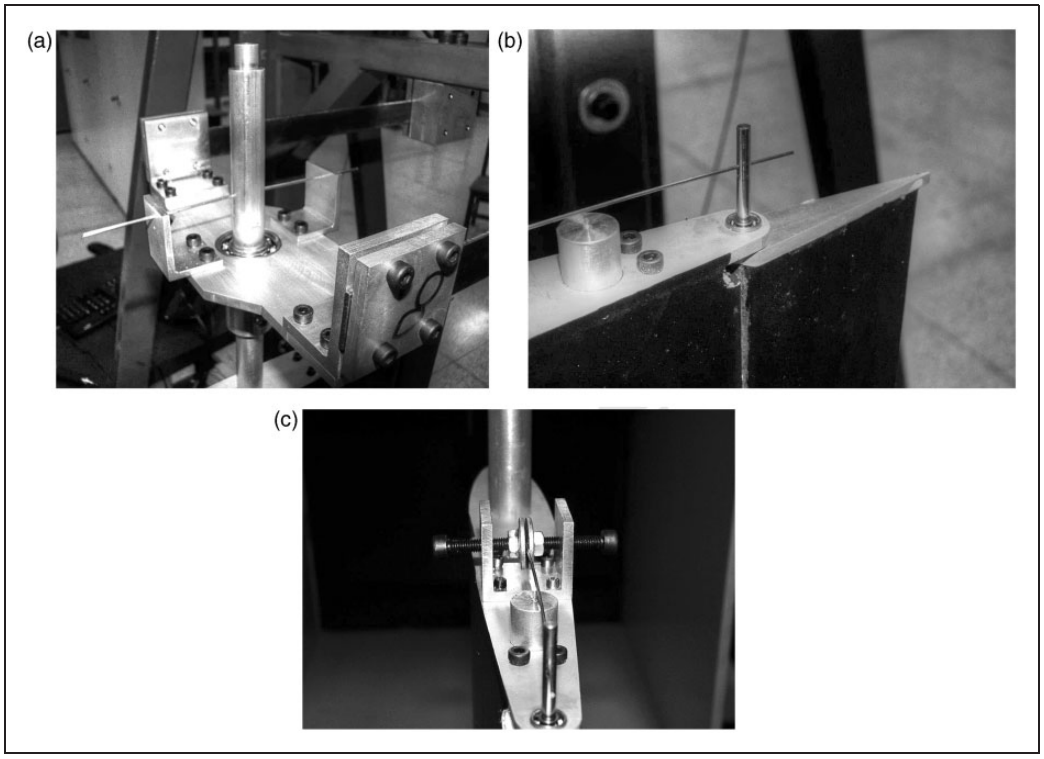

Figure 2. Details of the experimental apparatus: (a) pitch spring wire; (b) control surface spring wire; (c) control surface freeplay mechanism.

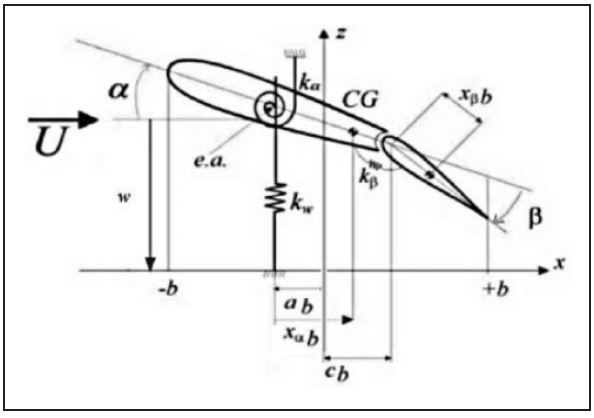

Figure 3. Typical aeroelastic section model.

$$M_\beta(t) = M_\beta^{(nc)} + M_\beta^{(c)}, \tag{4}$$

where the non-circulatory terms are

$$L^{(nc)} = \pi\rho b^2\left[\ddot{w} + U\dot{\alpha} - ab\ddot{\alpha} - \frac{U}{\pi}T_4\dot{\beta} - \frac{b}{\pi}T_1\ddot{\beta}\right], \tag{5}$$

$$M_\alpha^{(nc)} = \pi\rho b^2\left\{ab\ddot{w} - Ub\left(\frac{1}{2}-a\right)\dot{\alpha} - b^2\left(\frac{1}{8}+a^2\right)\ddot{\alpha} - \frac{U^2}{\pi}(T_4+T_{10})\beta + \frac{Ub}{\pi}\left[-T_1+T_8+(c-a)T_4-\frac{1}{2}T_{11}\right]\dot{\beta} + \frac{b^2}{\pi}[T_7+(c-a)T_1]\ddot{\beta}\right\}, \tag{6}$$

$$M_\beta^{(nc)} = \pi\rho b^2\left\{\frac{b}{\pi}T_1\ddot{w} + \frac{Ub}{\pi}\left[2T_9+T_1-(a-\frac{1}{2})T_4\right]\dot{\alpha} - \frac{2b^2}{\pi}T_{13}\ddot{\alpha} - \frac{U^2}{\pi^2}(T_5-T_4T_{10})\beta + \frac{UbT_4T_{11}}{2\pi^2}\dot{\beta} + \frac{b^2T_3}{\pi^2}\ddot{\beta}\right\}, \tag{7}$$

and the circulatory terms are

$$L^{(c)} = 2\pi\rho UbC(k)f(t), \tag{8}$$

$$M_\alpha^{(c)} = 2\pi\rho b^2\left(a+\frac{1}{2}\right)C(k)f(t), \tag{9}$$

$$M_\beta^{(c)} = -\rho Ub^2T_{12}C(k)f(t), \tag{10}$$

where $C(k)$ is the Theodorsen function and

$$f(t) = U\alpha + \dot{w} + \dot{\alpha}b\left(\frac{1}{2} - a\right) + \frac{U}{\pi}T_{10}\beta + \frac{b}{2\pi}T_{11}\dot{\beta}, \quad (11)$$

is the quasi-steady term and the T-functions are as defined by Theodorsen (1935).

The aerodynamic loads given from Equations (2)–(4) depend on the Theodorsen function $C(k)$, where $k = \omega b/U$ is the reduced frequency of harmonic oscillations. To simulate aeroelastic responses to arbitrary motions, the loads associated with Theodorsen function can be manipulated by convolution based on Duhamel formulation in the time domain (Li et al., 2010). If the Wagner function is also considered, it implies that, for instance, circulatory lift term can be written as

$$L^{(c)} = C(k)f(t) = f(0)\phi(\tau) + \int_0^\tau \frac{\partial f(\sigma)}{\partial \sigma}\phi(\tau - \sigma)\,\mathrm{d}\sigma, \quad (12)$$

where σ is a dummy integration variable, and $\phi(\tau)$ is Wagner function in the non-dimensional time $\tau = tU/b$, approximated by Sear's approach (Sears, 1940),

$$\phi(\tau) \approx c_0 - c_1 \mathrm{e}^{-c_2\tau} - c_3 \mathrm{e}^{-c_4\tau}, \quad (13)$$

where $c_0 = 1.0$, $c_1 = 0.165$, $c_2 = 0.0455$, $c_3 = 0.335$ and $c_4 = 0.3$.

Using integration by parts and following the state space method proposed by Lee et al. (1997, 2005) and Li et al. (2010), Equation (12) leads to a circulatory term as

$$L^{(c)} = (c_0 - c_1 - c_3)f(t) + c_2c_4(c_1 + c_3)\bar{x} + (c_1c_2 + c_3c_4)\dot{\bar{x}}, \quad (14)$$

where $\bar{x}$ and $\dot{\bar{x}}$ are augmented aerodynamic states.

Such formulation allows to assess a set of aeroelastic equations of motion given by

$$\left(\mathbf{M}_s - \mathbf{M}^{(nc)}\right)\ddot{\mathbf{x}} + \left(\mathbf{B}_s - \mathbf{B}^{(nc)} - \frac{1}{2}\mathbf{R}\mathbf{S}_2\right)\dot{\mathbf{x}} + \left(\mathbf{K}_s - \mathbf{K}^{(nc)} - \frac{1}{2}\mathbf{R}\mathbf{S}_1\right)\mathbf{x} - \mathbf{R}\mathbf{S}_3\mathbf{x}_a = \mathbf{0}, \quad (15)$$

where $\mathbf{x} = [\alpha \quad \beta \quad w/b]^{\mathrm{T}}$ and $\mathbf{x}_a = [\bar{x} \quad \dot{\bar{x}}]^{\mathrm{T}}$.

In the state space form, Equation (15) results in

$$\dot{\mathbf{X}} = \mathbf{A}(\mathbf{X})\mathbf{X}, \quad (16)$$

where, $\mathbf{X} = [\alpha \quad \beta \quad \frac{w}{b} \quad \bar{x} \quad \dot{\bar{x}}]^{\mathrm{T}}$.

Details of the matrices in Equations (15) and (16) are presented in the appendix.

4. Control surface freeplay representation

In the discontinuous representation to account for symmetric freeplay effect with respect to null control surface deflection, $F(\beta)$ in Equation (2) may be given by

$$F(\beta) = \begin{cases} \beta + \delta, & \text{if} \quad \beta < -\delta, \\ 0, & \text{if} \quad |\beta| \le \delta, \\ \beta - \delta, & \text{if} \quad \beta > \delta. \end{cases} \quad (17)$$

A different representation of the freeplay-related discontinuity can be provided by continuous functions. This is the case of using combinations of hyperbolic tangent functions to represent the restoring torque in the control surface due to β deflections (Vasconcellos et al., 2012). The mathematical formulation for this combination is given by

$$F(\beta) = \frac{1}{2}[1 - \tanh(\varepsilon(\beta + \delta))](\beta + \delta) + \frac{1}{2}[1 + \tanh(\varepsilon(\beta - \delta))](\beta - \delta), \quad (18)$$

where δ denotes freeplay boundary region, and ε is a variable which affects the smoothness of the function, thereby determining the accuracy of the approximation.

In Equation (18), as ε increases, the hyperbolic tangent function combination becomes more representative of the real freeplay effect. This feature can be seen in Figure 4 as obtained by using Equation (18), and for examples of hyperbolic tangent function combination for increasing ε values. Clearly, as ε goes to infinity, the representation for $F(\beta)$ leads to the real freeplay discontinuous effect.

5. Nonlinear analysis

As a reference for both experimental and numerical results, the respective flutter speeds are assessed. To attain the flutter condition, the freeplay effect is not considered, therefore the aeroelastic system is assumed to be linear. Admitting the aeroelastic parameters in Table 1, and no freeplay, the numerical solution of equations of motion reveals the instability at $U_f = 9.2\,\mathrm{m/s}$. During the wind tunnel tests for a representative typical section with no induced freeplay effect, the flutter condition has been observed at higher airspeed than that predicted for the prior numerical simulation. It can be inferred that nonlinearity is present in the suspension, thereby inducing LCO prior to instability onset. This can be observed and the flutter speed has

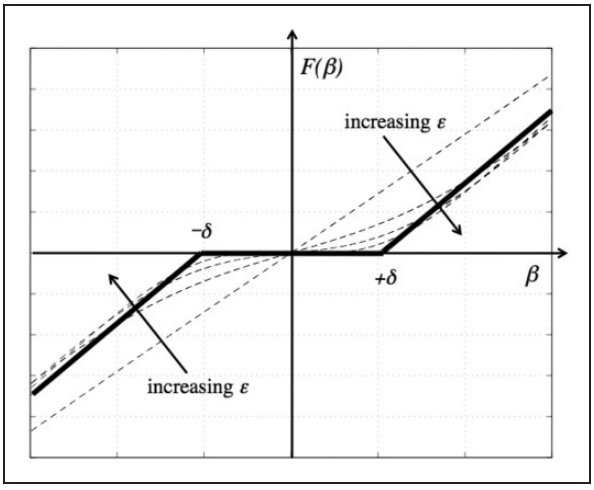

Figure 4. Control surface deflection *versus* torque described in Equation (18), ε increasing from 0 to 1000 (solid line would be an acceptable freeplay representation).

been detected at $U_f = 15.2\,\text{m/s}$. Flutter assessment during wind tunnel tests has been based on observing when aeroelastic response amplitudes increase at a particular airspeed. The flutter speed of $U_f = 15.2\,\text{m/s}$ represents an estimate when the aeroelastic system goes from dynamic stable responses to unstable ones.

An investigation into the suspension dynamics has been carried out, which reveals pronounced hardening effect at the pitching spring. Measurements have been made and a polynomial fit has been performed to obtain the most effective representation for this nonlinearity. In Figure 5 the discrete measurements of restoring pitching moment against pitching angle, together with the fifth-order polynomial fitting are depicted. When the polynomial function to account for the hardening effect is included in the numerical model, a better match to the flutter instability prediction is attained. The numerical model including polynomial fitting for the pitching moment restoring stiffness results in flutter speed of $U_f = 15.1\,\text{m/s}$. The reference flutter speeds are gathered in Table 2.

Experimental tests were carried out with an induced freeplay of $\approx 3.57^\circ$ at the control surface hinge (cf. Figure 2(c)). As consequence of including such nonlinearity, LCO characteristic self-sustained oscillations have been observed at airspeeds that are lower than the respective flutter airspeed. LCO onset has been verified at airspeeds around $U = 0.9U_f$. This condition persists until the maximum wind tunnel speed, that is $U \simeq 1.2U_f$.

Characterization of the experimental results using time series analysis techniques was then performed and this aided significantly in the investigation of nonlinear system properties (Marques and Vasconcellos, 2009). Each time series has been tested for stationarity and determinism using both *runtest* and *surrogate data test* (Kantz and Shreiber, 2004). Figures 6(a)–6(c) depict time histories of the control surface, pitch and plunge motions, respectively, for $U = 1.04U_f$. From those signals it is obvious that both pitch and plunge motions have periodic responses. On the other hand, complex motions are observed in the control surface motion, which is directly related to the freeplay effect. State space reconstruction of the control surface deflection time series was performed, using the SVD (singular value decomposition) method (Broomhead and King, 1986; Marques and Vasconcellos, 2009). SVD approach has revealed dimension three for this system, which means that reconstructed orbits in state space can be observed in a three-dimensional trajectory. Figure 7 presents the evolution of the reconstructed state space with increasing airspeed. The trajectories are restricted to two-dimensional projections ($c_{\beta 1}$ and $c_{\beta 2}$ in Figure 7) in order to help observe the most relevant aspects of the system dynamics. The shape of trajectories suggests LCOs with more than one dominant frequency. In previous works in the literature (Abdelkefi et al., 2011, 2012; Conner et al., 1996; Trickey et al., 2002; Vasconcellos et al., 2012), typical section with control surface freeplay is subjected to sub-critical bifurcation behavior. To test such condition, wind tunnel runs have been performed by progressively increasing the airspeed and collecting the time histories with respective LCO when it occurs. The same process is repeated, but now by progressively decreasing the airspeed. Using the root mean square (RMS) of the time history at each interval of time for a fixed airspeed, one can observe a bifurcation diagram that reveals the sub-critical behavior from different bifurcation paths if increasing or decreasing airspeeds. From the experimental tests for control surface RMS motion amplitudes, Figure 8(a) illustrates the sub-critical bifurcation and also confirms the LCO regime onset for $U = 0.9U_f$.

Numerical simulations have considered the typical section data from Table 1 and the measured freeplay of $\pm 3.57^\circ$, admitting the following damping matrix:

$$\begin{bmatrix} d_{\alpha\alpha} & d_{\alpha\beta} & d_{\alpha w} \\ d_{\beta\alpha} & d_{\beta\beta} & d_{\beta w} \\ d_{w\alpha} & d_{w\beta} & d_{ww} \end{bmatrix} = \begin{bmatrix} 1.3756 & 0.0185 & 2.3236 \\ 0.0185 & 0.0091 & 0.0259 \\ 2.3236 & 0.0259 & 5.5948 \end{bmatrix} (\text{kg/s}).$$

The control surface stiffness with freeplay has been represented by admitting combined hyperbolic tangent function (cf. Equation (18) and $\varepsilon = 1000$). Equation

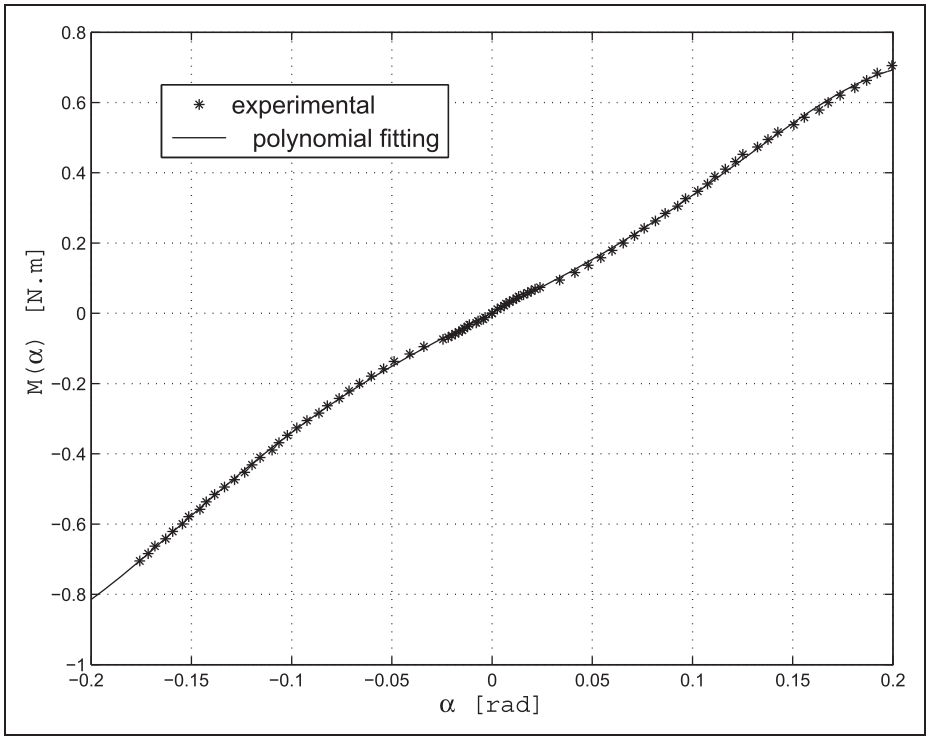

Figure 5. Experimental identification of the hardening stiffness nonlinearity in pitching (polynomial fitting: $M(\alpha) = -842.7\alpha^5 - 40.51\alpha^4 + 55.27\alpha^3 + 0.0673\alpha^2 + 2.906\alpha + 0.001508$).

Table 2. Numerical and experimental flutter speeds.

Numerical	Experimental
$U_f = 9.2$ m/s (linear)	$U_f = 15.2$ m/s
$U_f = 15.1$ m/s (with polynomial fitting)	

of motion integration using a traditional Runge–Kutta method has been performed over the range of experimental wind tunnel airspeeds. Figures 9(a)–9(c) show numerical and experimental time series when the freestream velocity is set equal to $1.04U_f$. It is clear that the hyperbolic tangent representation of the freeplay nonlinearity can simulate the complex control surface responses observed from experimental results. The good agreement between the proposed model and the experimental results for the pitch and plunge motions is also noted. These results also confirm the capabilities of using the hyperbolic tangent function combination to represent control surface freeplay that Vasconcellos et al. (2012) have verified with data retrieved from the literature.

Figure 10 serves to illustrate a comparison between a reconstructed trajectory from the experimental control surface response $\beta(t)$ at $1.04U_f$ with the respective case from numerical simulation. Numerical phase portrait is straightforward, therefore, the trajectories in Figure 10 can only be compared in a qualitative fashion. This result demonstrates once more a good agreement between numerical model with respect to experimental findings. Complex dynamics in LCO and frequency content has been reasonably captured by the numerical model.

Sub-critical bifurcation characterization can also be achieved from the numerical model. This fact can be confirmed by comparing the respective results. Figures 8(a) and 8(b) show, respectively, variations of the RMS control surface motion with the freestream velocity from measured experimental results and when numerical integrations based on the hyperbolic tangent representation of the freeplay nonlinearity were used. The results show that there are two distinctive regions for the system's response. In the first region, the control surface motion is damped when the freestream velocity is below $0.9U_f$. The second region is characterized by high response amplitudes and complex LCO, similarly to that reported by the experiments of Conner et al. (1996) and Trickey et al. (2002). There is a good agreement between numerical results and the experimental ones, reinforcing the applicability of hyperbolic tangent function combination to model control surface freeplay.

The power spectrum of the control surface motion for both experimental and numerical results is

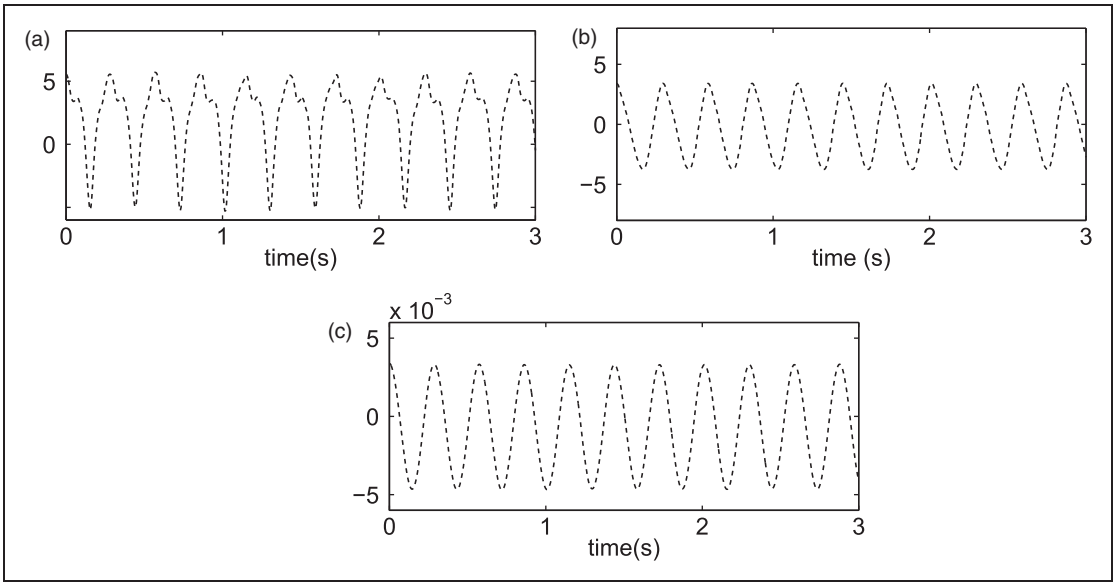

Figure 6. Experimental time series when $U = 1.04U_f$: (a) control surface response; (b) pitching response; (c) plunging response.

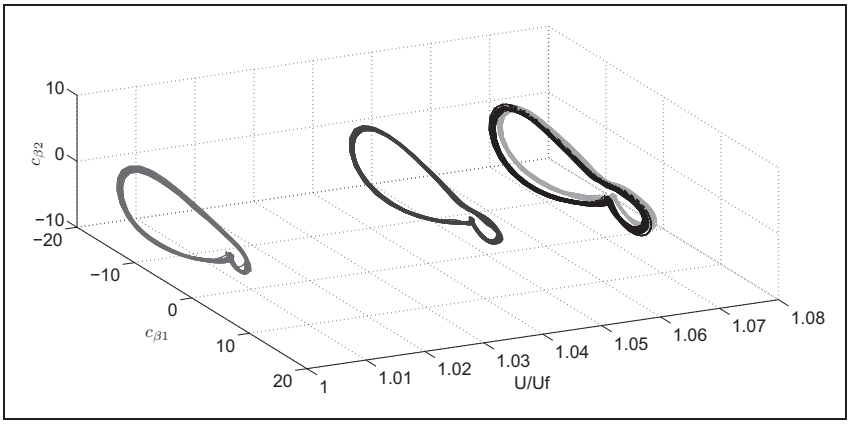

Figure 7. Control surface motion state space evolution with increasing freestream velocity from experimental data.

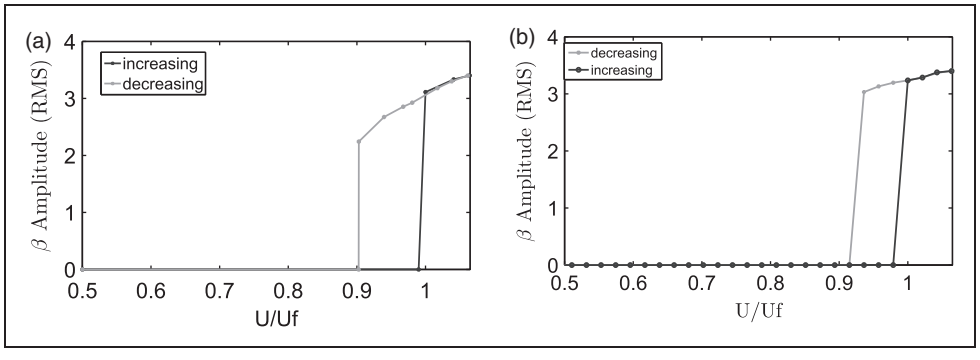

Figure 8. Bifurcation diagrams of control surface deflection RMS amplitudes when increasing and decreasing the wind speed: (a) experimental; (b) numerical model.

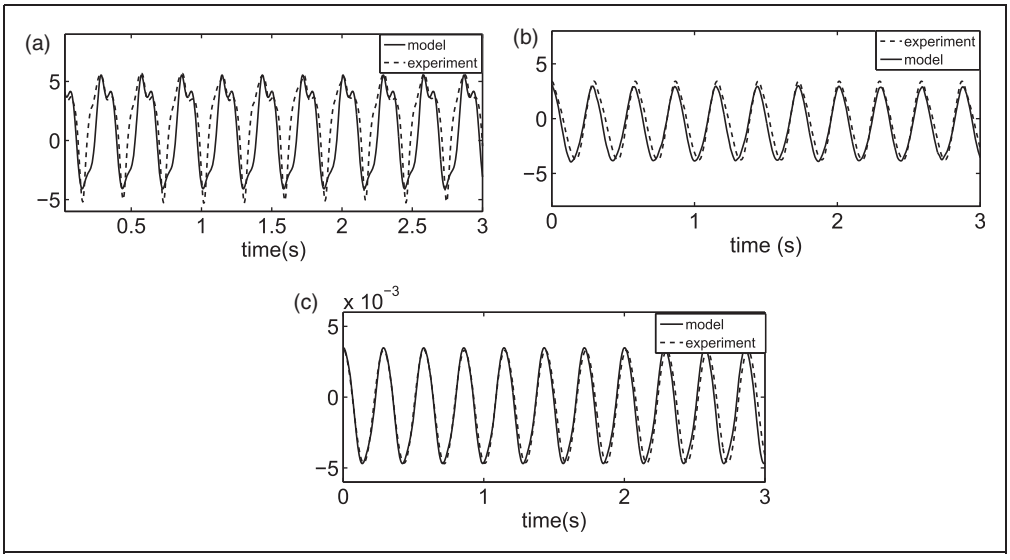

Figure 9. Aeroelastic time series comparison between numerical and experimental results when $U = 1.04U_f$: (a) control surface response; (b) pitch response; (c) plunge response.

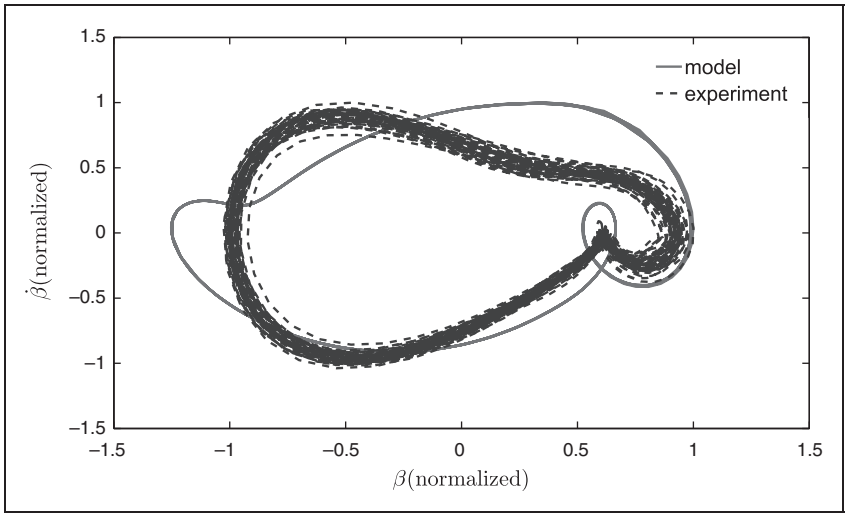

Figure 10. Control surface reconstructed trajectories at $U = 1.04U_f$: numerical and experimental (the normalization is with respect to the maximum measured values of β and $\dot{\beta}$).

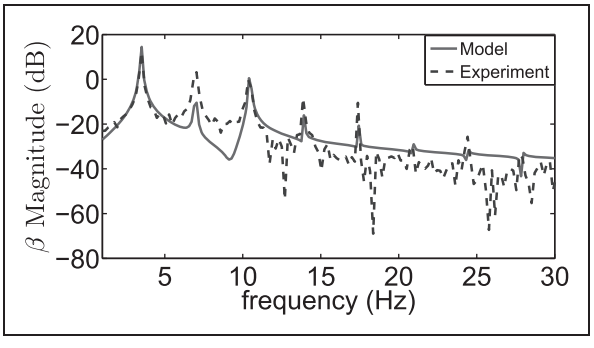

Figure 11. Power spectrum of the control surface response when $U = 1.04U_f$.

presented in Figure 11 for the case when the free-stream velocity is set equal to $1.04U_f$. It is noted that the amplitudes of the first and third harmonics are accurately predicted. The failure to predict the amplitude of the second harmonic implies that quadratic nonlinearities have not been adequately identified. It is most likely that there are other nonlinear effects, for instance, from bearings, friction, or even from aerodynamic sources, that should be included in the model. Nonetheless, the polynomial assumption for pitching stiffness nonlinearity has shown sufficient agreement in accounting for the main LCO dynamics for the freeplay problem.

6. Concluding remarks

An investigation of the use of hyperbolic tangent representation to model freeplay nonlinearity of a control surface has been performed and compared with experimental data. An experimental test in a wind tunnel was performed with an apparatus that is composed of a rigid airfoil supported by pitch and plunge elastic suspension with a control surface spring, capable of freeplay nonlinearity. Preliminary tests revealed that pitching spring behaved as hardening stiffness, therefore corrections to the numerical model were necessary to account for this kind of nonlinearity. A fifth-order polynomial fit was performed using a measured pitching restoring moment against pitch angle variation.

Experimental measurements with freeplay nonlinearities were performed, and aeroelastic signals were analyzed with time series techniques. After checking the basic signal properties, state space reconstruction using a SVD method was performed. The control surface motion has shown greater complexity when compared with the pitch and plunge motions. An inspection for bifurcation boundaries was also obtained from experiments. To check the existence of sub-critical bifurcation, the wind tunnel tests were executed following a progressive increase in airspeed until near flutter instability, and a progressive decrease in airspeed from near flutter. The respective bifurcation diagrams revealed the sub-critical condition.

The numerical model, after corrections for the hardening stiffness in pitch, revealed a flutter condition of approximately 64% higher than a linear typical section model. The corrected critical flutter speed from the numerical approach is 0.6% of the experimental one. This can be considered a satisfactory prediction admitting the other nonlinear effects are certainly present in the experimental device. The numerical model was capable of predicting the sub-critical bifurcation onset, as well as the LCO amplitude range. The overall performance of the numerical model based on hyperbolic tangent function combination for freeplay representation is very satisfactory.

Further investigations should consider the characterization of the other nonlinearities and dissipative effects of damping. It was observed that quadratic nonlinear effects require more attention in future work. This kind of problem may have origin from unsteady aerodynamic loading. A study on aeroelastic parameter changes (experimental and numerical) and the impact on nonlinear behavior is also under consideration.

Funding

This work was supported by the São Paulo State Research Agency, FAPESP, Brazil (grant number 2007/08459-1) and the Coordination for the Improvement of Higher Education Personnel (CAPES), Brazil (grant number 0205109). The authors are also thankful to the Brazilian Research Agencies, CNPq and FAPEMIG, for funding this present research work through the INCT-EIE (National Institute of Science and Technology in Smart Structures in Engineering).

References

Abdelkefi A, Vasconcellos RMG, Marques FD and Hajj MR (2011) Bifurcation analysis of an aeroelastic system with concentrated nonlinearities. *Nonlinear Dynamics* 69(1–2): 57–70.

Abdelkefi A, Vasconcellos RMG, Marques FD and Hajj MR (2012) Modeling and identification of freeplay nonlinearity. *Journal of Sound and Vibration* 331(8): 1898–1907.

Broomhead DS and King GP (1986) Extracting qualitative dynamics from experimental data. *Physica D* 20: 217–236.

Conner MD, Tang DM, Dowell EH and Virgin LN (1996) Nonlinear behavior of a typical airfoil section with control surface freeplay. *Journal of Fluids and Structures* 11: 89–109.

Fung YC (1993) *An introduction to the theory of aeroelasticity*. New York: Dover Publications.

Henon M (1982) On the numerical computation of Poincaré maps. *Physica D: Nonlinear Phenomena* 5(2–3): 412–414.

Jones DP, Roberts I and Gaitonde AL (2007) Identification of limit cycles for piecewise nonlinear. *Journal of Fluids and Structures* 23: 1012–1028.

Kantz H and Shreiber T (2004) *Nonlinear Time Series Analysis*, 2nd edn. Cambridge: Cambridge University Press.

Lee BHK and Tron A (1989) Effects of structural nonlinearities on flutter characteristics of the CF-18 aircraft. *Journal of Aircraft* 26: 781–786.

Lee BHK, Gong L and Wong YS (1997) Analysis and computation of nonlinear dynamic response of a two degree of freedom system and its application in aeroelasticity. *Journal of Fluids and Structures* 11: 225–246.

Lee BKH, Liu L and Chung KW (2005) Airfoil motion in subsonic flow with strong cubic nonlinear restoring forces. *Journal of Sound and Vibration* 281: 699–717.

Li D, Guo S and Xiang J (2010) Aeroelastic dynamic response and control of an airfoil section with control surface nonlinearities. *Journal of Sound and Vibration* 329: 4756–4771.

Marques FD and Vasconcellos RMG (2009) Chaotic patterns in aeroelastic signals. *Mathematical Problems in Engineering*, p. 19. doi: 10.1155/2009/802970.

Roberts I, Jones DP, Lieven NAJ, di Bernardo M and Champneys AR (2002) Analysis of piecewise linear aeroelastic systems using numerical continuation. *Proceedings of the Institution of Mechanical Engineers, Part G. Journal of Aerospace Engineering* 216(2): 1–11.

Sears WR (1940) Operational methods in the theory of airfoils in non-uniform motion. *Journal of the Franklin Institute* 230: 95–111.

Theodorsen T (1935) General theory of aerodynamic instability and the mechanism of flutter. *NACA Technical Report 496*.

Trickey T, Virgin LN and Dowell EH (2002) The stability of limit-cycle oscillations in an nonlinear aeroelastic system.

Proceedings: Mathematical, Physical and Engineering Sciences 458(2025): 2203–2226.

Vasconcellos RMG, Abdelkefi A, Marques FD and Hajj MR (2012) Modeling and analysis of control surface freeplay nonlinearity. *Journal of Fluids and Structures* 31(6): 79–91.

Virgin LN, Dowell EH and Conner MD (1999) On the evolution of deterministic non-periodic behavior of an airfoil. *International Journal of Nonlinear Mechanics* 34: 499–514.

Appendix: matrices of Equations (15) and (16)

Structural matrices:

$$\mathbf{M}_s = \begin{bmatrix} r_\alpha^2 & r_\beta^2 + (c-a)x_\beta & x_\alpha \\ r_\beta^2 + (c-a)x_\beta & r_\beta^2 & x_\beta \\ x_\alpha & x_\beta & \dfrac{m_T}{m_W} \end{bmatrix},$$

$$\mathbf{B}_s = \left(\Lambda^{\mathrm{T}}\right)^{-1} \begin{bmatrix} 2m_\alpha\omega_\alpha\zeta_\alpha & 0 & 0 \\ 0 & 2m_\beta\omega_\beta\zeta_\beta & 0 \\ 0 & 0 & 2m_w\omega_w\zeta_w \end{bmatrix} \Lambda^{-1},$$

$$\mathbf{K}_s = \begin{bmatrix} r_\alpha^2\omega_\alpha^2 & 0 & 0 \\ 0 & r_\beta^2\omega_\beta^2\dfrac{F(\beta)}{\beta} & 0 \\ 0 & 0 & \omega_w^2 \end{bmatrix},$$

where Λ is the eigenvector matrix from $\mathbf{M}_s\ddot{\mathbf{x}} = -\mathbf{K}_s\mathbf{x}$ and m_α, m_β, m_w are modal masses.

Non-circulatory and circulatory aerodynamic matrices:

$$\mathbf{M}^{(nc)} = -\frac{\rho}{m_W}\begin{bmatrix} \pi b^2\left(\dfrac{1}{8}+a^2\right) & -[T_7+(c-a)T_1]b^2 & -\pi ab^2 \\ 2T_{13}b^2 & -T_3b^2/\pi & -T_1b^2 \\ -\pi ab^2 & -T_1b^2 & \pi b^2 \end{bmatrix},$$

$$\mathbf{B}^{(nc)} = -\frac{\rho}{m_W}\begin{bmatrix} \pi\left(\dfrac{1}{2}-a\right)Ub & \left[T_1-T_8-(c-a)T_4+\dfrac{T_{11}}{2}\right]Ub & 0 \\ \left[-2T_9-T_1+T_4\left(a-\dfrac{1}{2}\right)\right]Ub & \dfrac{-T_4T_{11}Ub}{2\pi} & 0 \\ \pi Ub & -UT_4b & 0 \end{bmatrix},$$

$$\mathbf{K}^{(nc)} = -\frac{\rho}{m_W}\begin{bmatrix} 0 & (T_4+T_{10})U^2 & 0 \\ 0 & \dfrac{(T_5-T_4T_{10})U^2}{\pi} & 0 \\ 0 & 0 & 0 \end{bmatrix},$$

$$\mathbf{R} = \frac{1}{m_W}\begin{bmatrix} 2\pi\rho U\left(a+\dfrac{1}{2}\right) & -\rho UT_{12} & -2\pi\rho U \end{bmatrix}^{\mathrm{T}},$$

$$\mathbf{S}_1 = \begin{bmatrix} U & \dfrac{T_{10}U}{\pi} & 0 \end{bmatrix},$$

$$\mathbf{S}_2 = \begin{bmatrix} b\left(\dfrac{1}{2}-a\right) & \dfrac{bT_{11}}{2\pi} & b \end{bmatrix},$$

$$\mathbf{S}_3 = \begin{bmatrix} \dfrac{c_2c_4(c_1+c_3)U^2}{b} & (c_1c_2+c_3c_4)U \end{bmatrix},$$

where ρ is the air density.

State matrix:

$$\mathbf{A}(\mathbf{X}) = \begin{bmatrix} \mathbf{0} & \mathbf{I} & \mathbf{0} \\ -\mathbf{M}_t^{-1}\mathbf{K}_t & -\mathbf{M}_t^{-1}\mathbf{B}_t & -\mathbf{M}_t^{-1}\mathbf{D} \\ \mathbf{E}_1 & \mathbf{E}_2 & \mathbf{F} \end{bmatrix},$$

where

$$\mathbf{M}_t = \left(\mathbf{M}_s - \mathbf{M}^{(nc)}\right), \quad \mathbf{B}_t = \left(\mathbf{B}_s - \mathbf{B}^{(nc)} - \frac{1}{2}\mathbf{R}\mathbf{S}_2\right),$$

$$\mathbf{K}_t = \left(\mathbf{K}_s - \mathbf{K}^{(nc)} - \frac{1}{2}\mathbf{R}\mathbf{S}_1\right), \quad \mathbf{D} = \mathbf{R}\mathbf{S}_3,$$

$$\mathbf{E}_1 = \begin{bmatrix} 0 & 0 & 0 \\ \dfrac{U}{b} & \dfrac{UT_{10}}{\pi b} & 0 \end{bmatrix},$$

$$\mathbf{E}_2 = \begin{bmatrix} 0 & 0 & 0 \\ \left(\dfrac{1}{2} - a\right) & \dfrac{T_{11}}{2\pi} & 1 \end{bmatrix},$$

$$\mathbf{F} = \begin{bmatrix} 0 & 1 \\ \dfrac{-c_2 c_4 U^2}{b^2} & \dfrac{-(c_2 + c_4)U}{b} \end{bmatrix}.$$